mathematics

MDPI

*Article*

# Mathematical Modeling and Dynamic Simulation of Frog Jumping for Bio-Inspired Robotics

**Nuria Sánchez Pérez [1,2] and Juan David Cano-Moreno [1,*]**

[1] Escuela Técnica Superior de Ingeniería y Diseño Industrial, Universidad Politécnica de Madrid, 28012 Madrid, Spain; nuria.sanchezp@alumnos.upm.es
[2] Faculty of Industrial Design Engineering, Delft University of Technology, Landbergstraat 15, 2628 CE Delft, The Netherlands
* Correspondence: juandavid.cano@upm.es

**Abstract**

The biomechanics of frog jumping has been a subject of significant interest in both biology and engineering, driven by the high efficiency of their movement. This study presents the dynamic simulation of a frog's complete jump cycle, from take-off to landing and re-stabilization, to advance the development of bio-inspired jumping robots for irregular terrains. As a primary contribution, and unlike previous studies that focus exclusively on the propulsion phase, this work addresses all stages, using direct servomotor actuation without mechanical energy storage. Biological joint kinematics were mathematically characterized using Cubic Smoothing Splines. By empirically tuning the smoothing parameter ($p$), the trajectories achieved the continuous differentiability required for electromechanical actuation. These curves were implemented into a 3D multibody simulation (Altair Inspire), where a PID-based tracking framework managed the mechanically nonlinear multibody dynamics governing the jump (arising from contact forces, impacts, and time-varying inertial effects) to ensure stabilization during the complex landing phase. Validating the model against previous studies, the simulation successfully achieved a maximum horizontal jump distance of 24.12 cm (4.02 body lengths) and a peak velocity of 1.45 m/s. The kinematic fidelity of the model was mathematically validated, yielding a maximum Normalized Root Mean Square Error (NRMSE) of 4.121% relative to biological reference trajectories. Furthermore, the robustness of the landing and re-stabilization phases was demonstrated through a continuous double jump covering a total distance of 45.83 cm. Finally, a dynamic scaling analysis was performed to evaluate the feasibility of implementing real motors. Ultimately, this study establishes a mathematically robust framework for replicating frog-inspired jumping dynamics, contributing a transferable methodology for the design and control of articulated bio-inspired robotic systems.

**Keywords:** bio-inspired robotics; frog-inspired locomotion; kinematic trajectory modeling; cubic smoothing splines; dynamic simulation; PID controller; multibody dynamics; biomechanics

**MSC:** 70E60; 92C10; 65D07

Check for updates

Academic Editors: José Leonel Linhares da Rocha and Tongxing Li

Received: 26 March 2026
Revised: 15 April 2026
Accepted: 21 April 2026
Published: 23 April 2026

**Copyright:** © 2026 by the authors. Licensee MDPI, Basel, Switzerland. This article is an open access article distributed under the terms and conditions of the Creative Commons Attribution (CC BY) license.

## 1. Introduction

Biomimetics, also known as bionics or bio-inspired design, is a discipline based on the premise that nature, through millions of years of evolution, has already resolved many of the problems faced in engineering. Instead of reinventing solutions, this field

observes living organisms to translate their principles into technology. However, translating biological observations into robotic systems presents a mathematical and control challenge. The raw kinematic data extracted from living organisms is inherently discrete and noisy for direct electromechanical actuation. If biological trajectories are not rigorously formalized mathematically, small discontinuities in position or velocity will theoretically demand infinite instantaneous accelerations from the actuators, leading to mechanical instability.

To address this, a core contribution of this work lies in the mathematical formulation of Cubic Smoothing Splines to characterize biological locomotion. By applying this mathematical framework, the discrete biological datasets are transformed into continuously differentiable ($C^2$) functions. Moreover, tuning the smoothing parameter $p$ modifies the temporal stability of these functions, filtering biological noise while preserving essential kinematic amplitudes [1,2]. With these smooth trajectories established, the connection between linear PID trajectory tracking and the highly non-linear dynamics of the multibody system was explored. This was done to demonstrate that mathematically formalized inputs enable a continuous PID feedback loop to stabilize rapid inertia changes and impact forces, particularly during landing, thereby bypassing the unpredictable dynamics of traditional elastic energy storage. To contextualize this mathematical approach, a historical review of bio-inspired engineering is essential.

The roots of biomimetics trace back to over 3000 years ago, with examples such as the creation of artificial silk in ancient China, Leonardo da Vinci's study of bird flight, and the organic aesthetic of the Art Nouveau movement. However, it was formalized in the mid-20th century as a form of understanding the functions of biological systems to synthesize artificial products [3]. In recent decades, this field has experienced significant growth, driven by the need for sustainable and innovative solutions, since nature provides unlimited inspiration to solve complex problems.

One of the most popular examples is the hydrophobic "lotus effect", which relies on the crown morphology of the plant's papillae. Scientists have replicated this microstructure to develop self-cleaning and water resistant coatings for textiles, solar panels, and buildings [4,5]. The invention of Velcro by George Mestral in 1941 was inspired by the mechanical adhesion observed in burdock seeds, since they feature microscopic hooks that attach to passing fabrics [4]. Furthermore, in the context of locomotion, biological adhesion has been extensively studied in geckos. These animals use a completely dry adhesion mechanism to scale up vertical surfaces. Their toes are covered with millions of microscopic structures called lamellae that branch into smaller parts, exponentially increasing the contact area. This hierarchy allows geckos to support their own weight through Van der Waals forces, providing a dynamic and reversible adhesion mechanism that leaves no residue, a principle currently being explored for climbing and rescue robots [4,6,7].

In the realm of aerodynamics and fluid dynamics, some natural systems have provided inspiration to improve the efficiency of machines. The structure of bird wings inspired the development of winglets in aviation to minimize the formation of drag vortices. Aquatic animals have been used to improve the hydrodynamic efficiency of vessels; for example, shark dermal denticles include longitudinal grooves that channel water and reduce turbulent vortices. Therefore, the boundary layer separation is more controlled, which lowers the friction coefficient [4,8]. The automotive industry has also benefited from aquatic biomimetics, as seen in the Mercedes-Benz Bionic Concept Car, which was modeled after the boxfish (*Ostracion meleagris*). Despite its angular appearance, the boxfish moves rapidly with minimal drag, a principle successfully transferred to the vehicle's highly aerodynamic chassis [4,9].

These examples demonstrate the historical success of biomimicry, although the field is rapidly expanding into all engineering domains, including robotic adaptation. Recent

advancements in 2025 have pushed these boundaries further; for instance, researchers have developed dome architectures inspired by the microscopic chorion of Lepidopteran insect eggs, which enhance the mechanical stability and pressure resistance of 3D-printed shells [10]. In the field of soft robotics, a milestone has been achieved with the transition from rigid propeller to cable-driven limbs. These allow mobility in complex marine terrains due to the development of bipedal underwater robots [11].

Within this broader context of bio-inspired engineering, the study of biological locomotion provides critical insights for robotic mobility. Jumping is a capability that has been perfected by numerous species to navigate obstacles and vertical differences. While some animals combine jumping with flight or walking, for many, like frogs, it is a primary or intermittent mode of displacement crucial for survival.

### *1.1. Classification of Bio-Inspired Jumping Mechanisms*

The exploration of bio-inspired jumping mechanisms began with NASA's 1969 Apollo project, which conceptualized a lunar jumping robot to efficiently navigate low gravity. By the 1980s, early prototypes like the 3D Hopper and the Acrobot used simple two-degree-of-freedom double pendulum systems to manage propulsion and landing [12]. To further develop these technologies, researchers categorized jumping mechanisms to better replicate the diverse locomotion of terrestrial vertebrates and invertebrates, generally excluding aquatic swimming dynamics from these specific models [13].

In modern robotics, jumping mechanisms are generally classified into SLIP (Spring-Loaded Inverted Pendulum) models and linkage mechanisms (open or closed chains). The SLIP model, consisting of a spring and a mass point, offers high power density due to its simplicity and low degrees of freedom, but it can be unstable and difficult to control during landing [12]. On the contrary, multi-link mechanisms, which are used in more complex bio-inspired robots, attempt to more accurately simulate the complex biomechanical behaviors of animals. These mechanisms allow for adjustment of the take-off angle, landing control, and greater flexibility of movement, despite their higher mathematical modelling complexity.

### *1.2. Energy Storage and Actuation*

Since effective jumping requires rapid release of energy, robots have adopted various biomechanical strategies that animals use to jump. Several general jumping methods have been classified.

1. Energy storage: Many systems employ linear or torsional springs to act as tendons, accumulating energy that is later released rapidly. The elastic energy stored in these springs is directly proportional to the spring constant $k$ and the deformation $x$, defined by the equation $E = \frac{1}{2}kx^2$. For example, the "JumpRoACH" uses latex bands within a diamond-shaped linkage, and the degree of extension can be adjusted by a motor [14]. The locust-inspired robot developed by Mirko Kovac uses a motor driven cam to load a torsion spring. The cam's profile acts as a click mechanism, instantly releasing the stored energy when maximum extension is reached. This mechanism allowed the 7 g robot to achieve a height of jump of 27 times its height [12,13,15].
2. Pneumatic Actuation: Robots like the "Arachnabot" or soft pneumatic robots use compressed air cylinders or inflatable chambers. In the test experiments of the "Arachnabot", the robot showed impressive actuating speed, fulfilling a leg extension in 17 milliseconds and a vertical jump up to 11.5 cm [16]. Moreover, by using four independent actuators per leg, the airflow timing can be manipulated to control the jump direction [17]. Although precise, these systems are often bulky and less efficient than elastic springs [12].

3. Shape Memory Alloys (SMAs): Some materials like nitinol can recover their shape after deforming due to thermal changes, transitioning from a flexible martensitic phase to a rigid austenitic phase when heated. Because of their high power-to-weight ratio, these actuators are ideal for miniature robots, where size and weight are critical constraints. In the flea-inspired robot [18], an SMA actuator is used in a simple four-bar mechanism to obtain the jumping movement once the energy from the SMA is released. Similarly, a robot inspired by the froghopper (*Cercopoidea*) utilizes an SMA spring for explosive acceleration. To prevent the robot from spinning out of control during the jump, a conventional gear set synchronizes the hind legs, ensuring that the rotational moments generated by each leg mutually cancel out (see Equation (1)). Nevertheless, these actuators suffer from slow responses and are sensitive to thermal changes [12,19].

$$L_{\text{tibia}} F_{G_x} \cos(\theta) - L_{\text{tibia}} F_{G_y} \sin(\theta) = 0 \quad (1)$$

4. Combustion: Some robots use hydrocarbon (like butane) combustion for explosive power. In the 'untethered soft robot' [20], combustion is used in three different legs to change the center of mass and control the direction. Although this method is powerful and fast, the nature of the explosiveness of the reaction makes it difficult to apply.

In Table 1 below, a summary of the most relevant bio-inspired jumping robots analyzed are represented regarding the mechanism implemented, components, and weaknesses.

**Table 1.** Analysis of bio-inspired jumping robots.

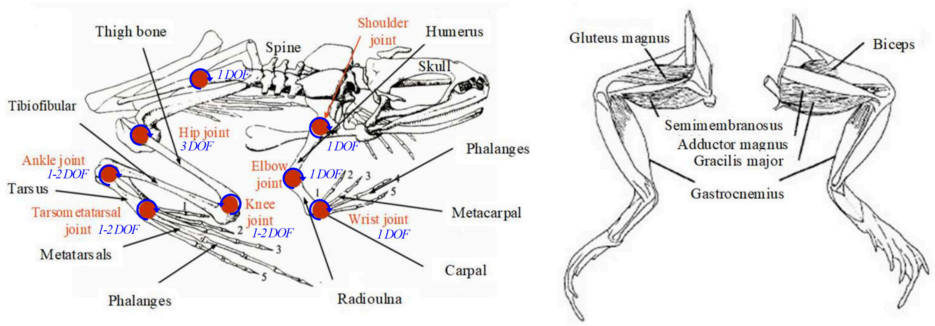
| Energy Storage Type | Mechanism | Robot Example | Components | Weaknesses |
|---|---|---|---|---|
| Elastic | Linear spring<br>Latex band/torsion spring | Locust-inspired JumpRoACH/7 g Hopper | Cam, cable, springs<br>Latex bands, gear systems, cams | Mechanism complexity<br>Control of landing and direction |
| SMA | SMA spring | Flea-inspired | Four-bar link, SMA spring, trigger | Slow thermal response |
| Pneumatic | Pneumatic cylinder | Arachnabot | Actuators, membranes, cables | Dependence on pressure/valves |
| Combustion | Butane | Untethered | Piston actuators, spark ignition | Explosive control difficulty |

### *1.3. Frog Morphology and Kinematics*

The anatomical structure of frogs, represented in Figure 1, is characterized by a musculoskeletal particularly suitable for powerful and rapid movements. The morphology consists of the head (flat and pointed to reduce drag), the torso (where mass is concentrated), and the limbs. The hind limbs are long and muscular to generate propulsion, while the forelimbs are shorter, responsible for absorbing landing impact and orienting the movement [21].

The skeletal structure of the hind limbs includes the femur, tibiofibula, tarsus, and metatarsus/phalanges. These are connected by joints with specific degrees of freedom (DOFs) [21]:

- Knee, ankle, and metatarsus: These joints primarily facilitate flexion and extension. Although they can be modelled with just one or two DOFs, they play an essential role in energy transfer during the jump.
- Hip: It is a spherical joint providing three DOFs (flexion/extension, abduction/adduction, internal/external rotation).
- Shoulder, elbow, and wrist: The shoulder acts as a spherical joint, while the elbow and wrist function as hinge joints (one DOF) to stabilize the body.




(**a**) (**b**)

**Figure 1.** (**a**) Skeletal structure of the frog with key biological joints highlighted (red dots). The specific degrees of freedom (DOFs), representing how these joints are typically modeled in the literature, have been added in blue [21]. (**b**) Major muscular anatomy governing the propulsive and landing phases.

Moreover, the hind limb musculature of frogs, particularly the semimembranosus, gastrocnemius, and biceps femoris, plays a fundamental role in the biomechanics of jumping. These muscle groups operate synergistically alongside their associated tendons to function as a biological catapult system. During the preparatory crouch phase, these muscles contract to stretch the elastic connective tissues, storing significant amounts of mechanical energy [21,22].

### *1.4. Phases of the Jump*

The jump is composed of three distinct stages: take off, aerial phase, and landing [21]. These phases can be visualized in Figure 2.

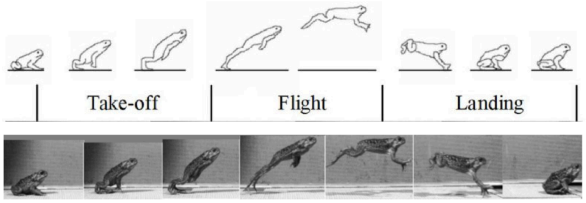



**Figure 2.** Phases of a frog's jump [23,24].

During the take-off phase, the frog begins in a crouched position with the hind limbs fully flexed at an acute angle and the metacarpals touching the ground. The hind limb muscles contract explosively. As the legs extend, the torso elevates, and the forelimbs shift to adjust the exit angle.

In the aerial phase, the hind limbs remain extended to maximize the moment of inertia and stability. Simultaneously, the forelimbs stretch forward to adjust the direction and prepare for impact.

Lastly, during the landing phase, the forelimbs contact the ground first, lowering the center of gravity. The hind limbs then retract rapidly to stabilize the body for the next cycle [21].

### *1.5. Review of Previous Structural Models*

The scientific literature reviewed presents various structural models based on different species, including the leopard frog, *Rana pipiens*, *Rana nigromaculata*, and the bullfrog, each offering specific insights into the optimization of jumping mechanics.

In the analysis of the leopard frog using ADAMS 2024 and SolidWorks 2026 software, four distinct models were established with varying degrees of freedom (DOFs) to evaluate their influence on jump efficiency. The most complex structure, "Model 1," incorporated

nine DOFs, including three at the hip for flexion, abduction, and rotation. This model achieved the greatest horizontal distance of 0.34 m. In contrast, the simplified "Model 4," which restricted movement to a single plane with only six DOFs, resulted in a significantly reduced jump distance of 0.14 m, demonstrating that a higher number of degrees of freedom allows for more flexible movements and better performance. However, increased complexity demands higher torque; consequently, "Model 3" (seven DOFs) was identified as the most balanced alternative, achieving a jump distance of 0.28 m with a lower maximum torque requirement of 12.5 Nmm compared to the 13.2 Nmm required by Model 1 [21].

Research regarding *Rana pipiens* used reverse engineering and 3D scanning to explore the interaction between skeletal biomechanics and neuromuscular function. Through the simulation of different kinematic configurations, it was determined that internal knee rotation is a critical factor for maximizing jump distance, as it allows the frog to position its feet under its body during the propulsive phase. The study concluded that the most effective model was one that included nine DOFs and an additional tarsometatarsal joint, which achieved a jump length of 0.704 m and a take-off velocity of 1.98 m/s, closely matching the performance of the biological frog [25].

Further investigations into *Rana pipiens* employed high-speed videography at 100 frames per second to analyze joint trajectories. This led to the development of mechanical models using four-bar and five-bar linkages with springs. While the four-bar mechanism simplified the hind limb structure to maintain a direct relationship between applied force and extension, the subsequent five-bar linkage model introduced a gear system to coordinate leg retraction, allowing for jumps of up to 1.12 m in distance [23,25].

Finally, bio-inspired robotics based on the bullfrog focused on mass distribution, concentrating weight in the torso to minimize limb inertia. This approach utilized a six-bar Stephenson mechanism to generate a linearized jump trajectory, successfully achieving a horizontal distance of 1.1 m [24].

In the table below, the different measurements and results obtained are compared to the literature analyzed in Table 2.

**Table 2.** Summary of data collected in the literature review.

| Study | Weight (g) | Femur (mm) | Tibia (mm) | Tarsus | Max. Distance (m) | Max. Velocity (m/s) |
|---|---|---|---|---|---|---|
| *Leopard frog* | 22 | 28 | 27.5 | 15 | 0.34 | 1.06 |
| *Pipiens frog* | 22 | 26.8 | 30.7 | 15.4 | 0.7 | 1.98 |
| *Nigromaculata* | 21.98 | 31.35 | 31.35 | 15.68 | 1.12 | N/A |
| *Bullfrog* | 500 (robot) | 100 | 105 | N/A | 1.1 | 2.5 |

### *1.6. Problem Statement and Research Gap*

Recent literature continues to explore diverse actuation methods to replicate frog jumping, predominantly relying on energy storage. For instance, "Bionics-Based Research on Frog-Jumping Robots" uses a motor driven gear and spring mechanism to provide elastic force [26]. Exploring alternatives that do not use mechanical springs, the study by Zhong et al. [27] employs pneumatic muscle actuators. Notably, while this study uses a PID controller, it strictly regulates pneumatic pressure rather than direct joint kinematics. Similarly, the study developed by the Harbin Institute of Technology (HIT) utilizes a highly explosive hydrogen–oxygen detonation drive [28].

While these related studies demonstrate excellent take-off velocities and high power-to-weight ratios, a fundamental problem remains: systems relying on instantaneous energy release suffer from unpredictable dynamics. This makes continuous trajectory control and stabilization during the landing phase difficult. Existing approaches optimize heav-

ily for propulsion but lack the mechanical continuity required to manage multi-phase jump stability.

Despite these creative advancements in mechanical, pneumatic, and chemical actuation, a significant gap remains in the literature: none of these models simulate jumping kinematics (from take-off through landing) using pure servomotor actuation without energy storage. This project directly addresses that gap by exploring the replication of biological kinematic curves through the direct application of servomotors, offering precise position and angular velocity regulation with PID controllers to propose a simpler simulation of the landing phase, and an energy-storage-free robotic system.

In robotics, these actuators integrate an electric motor, a sensor, and a controller to continuously adjust their position based on external reference signals [29].

Position control is typically achieved through Pulse Width Modulation (PWM), where the duty cycle ($D$), which dictates the rotation angle ($\theta$), is defined by the ratio between the pulse duration ($T_{on}$) and the total period ($T$) and can be seen in Equation (2):

$$D = \frac{T_{on}}{T};\ \theta = k \cdot D \tag{2}$$

where $k$ represents a specific characteristic constant of the servomotor. To ensure precise trajectory tracking, these motors frequently employ PID (Proportional–Integral–Derivative) controllers. A PID controller minimizes the error $e(t) = r(t) - y(t)$ between the desired reference position r(t), which in this study corresponds to the continuously differentiable kinematics curves generated from the biological data, and the actual position y(t) by combining three main parameters: proportional gain ($K_P$), integral gain ($K_I$), and derivative gain ($K_D$) [30,31]. The total control signal $u(t)$ applied to the motor is the sum of the proportional, integral, and derivative corrections shown in the Equation (3) below [30]:

$$u(t) = K_P \cdot e(t) + K_I \int_0^t e(\tau)d\tau + K_D \cdot \frac{de(t)}{dt} \tag{3}$$

By using this continuous feedback loop, the system can dynamically correct deviations, anticipating future variations and compensating for accumulated errors. To ensure that the locomotion is coordinated, all independent joint trajectories are tracked simultaneously by a unified simulation clock. In this study, the PID controller is primarily used as a numerical tool to enable stable trajectory tracking within the nonlinear multibody simulation, rather than as an object of classical control design [32]. Since the system tracks continuously smoothed biological curves rather than step-like reference inputs, standard transient performance metrics (such as steady-state error calculations, rise time, overshoot, or settling time) are not applicable. To enforce this tracking within the solver (Altair Inspire 2024), the specific controller gains ($K_p$, $K_i$, and $K_d$) are implemented. Due to the high-velocity impact dynamics, the integral gain is intentionally set to zero ($K_i = 0$) to prevent steady-state error accumulation during the rapid kinematic transitions. To ensure continuous splines without destabilizing the solver during the landing impacts, gains of high magnitude are applied: a proportional gain ($K_p$) of $1.0 \times 10^8$ Nm/rad, and a derivative gain ($K_d$) of $5.0 \times 10^6$ Nms/rad. This mathematical approach guarantees that the robotic joints can accurately mimic the complex, non-linear angular kinematics observed during the frog's jump. It should be noted that this PID control is implemented purely computationally within the multibody solver, without the need for explicit mechatronic block diagrams or Simulink models.

The remainder of this paper is organized as follows: Section 2 details the methodology, including the extraction of biological kinematic data, its mathematical characterization using Cubic Smoothing Splines, and the configuration of the multibody dynamic simula-

tion. Section 3 presents the quantitative results of the simulation, validating the kinematic fidelity, the jump distance, and the stabilization of the landing phase. Section 4 discusses the implications of these findings, addresses the methodological limitations, and evaluates the feasibility of dynamic scaling for real motors. Finally, Section 5 outlines the main conclusions and proposes future directions for physical prototyping and experimental validation.

## 2. Materials and Methods

### *2.1. Morphological Data Extraction and Interpolation*

For the dynamic model in this study, the dimensions represented in Table 3 were extracted primarily from the Leopard frog study [21] using the simplified 6-DOF structure from Model 4 to facilitate an initial replication and validate the model. The model can be seen in Figure 3.

**Table 3.** Dimensions of the simulation model.

| Parameter | Torso | Femur | Tibia | Tarsus | Metatarsus |
|---|---|---|---|---|---|
| Length | 45 mm | 28 mm | 27.5 mm | 15 mm | 25 mm |

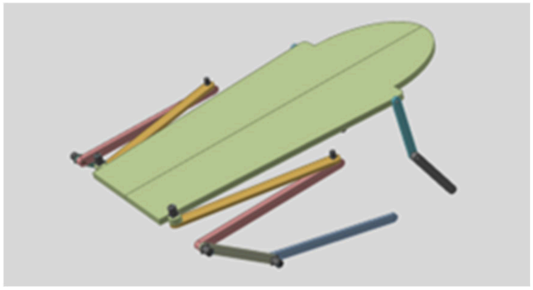


**Figure 3.** Replicated model of the Leopard frog in Altair.

To ensure the reproducibility of the initial posture, the spatial coordinates of each modeled joint are explicitly defined in Table 4. These coordinates were measured relative to the right metatarsus joint, which served as the local geometric origin (0, 0, 0) for the multibody system.

**Table 4.** Initial spatial coordinates of the modeled joints relative to the right metatarsus joint.

| | Metatarsus (mm) | | Ankle (mm) | | Knee (mm) | | Hip (mm) | | Shoulder (mm) | | Elbow (mm) | |
|---|---|---|---|---|---|---|---|---|---|---|---|---|
| | Right | Left | Right | Left | Right | Left | Right | Left | Right | Left | Right | Left |
| X | 0 | 0.000 | −12.326 | −12.326 | 12.267 | 12.270 | −12.192 | −12.504 | 35.808 | 35.808 | 31.035 | 31.035 |
| Y | 0 | 37.801 | 0.000 | 37.801 | 1.000 | 36.801 | 7.729 | 30.072 | 3.904 | 33.897 | 3.492 | 34.309 |
| Z | 0 | 0.000 | 5.748 | 5.748 | 12.202 | 12.202 | 6.492 | 7.959 | 17.717 | 17.717 | 7.654 | 7.654 |

For instance, the knee joint data was fitted to a 3rd-degree polynomial with an $R^2 = 0.9998$, to ensure high fidelity to the biological movement.

#### 2.1.1. Mathematical Characterization of Kinematic Trajectories

The raw kinematic data extracted from biological frog jumps is inherently subject to high frequency noise and discrete sampling artifacts. For the successful implementation into a physical robotic model, the input trajectories must be continuously differentiable. To resolve this, the biological angular trajectories were mathematically characterized and smoothed using Cubic Smoothing Splines [1,2]. Given a set of $n$ discrete biological data points $(t_i, y_i)$, where $t_i$ represents time and $y_i$ represents the joint angle, the smoothing

spline S(t) is defined as the function that minimizes the following composite objective functional, as shown in Equation (4) below:

$$L(S) = p\sum_{i=1}^{n} w_i(y_i - S(t_i))^2 + (1-p)\int_{t_1}^{t_n}\left(\frac{d^2S(t)}{dt^2}\right)^2 dt \quad (4)$$

The functional L(S) consists of two competing terms governed by the smoothing parameter $p \in [0,1]$. The first term represents the fidelity to the biological data (the weighted residual sum of squares), where $w_i$ is the specified error weights. The second term constitutes a roughness penalty, corresponding to the integral of the squared second derivative [33].

When $p = 0$, the penalty term dominates, yielding a least-squares linear regression. Conversely, when $p = 1$, the fidelity term dominates, resulting in a natural cubic spline that strictly interpolates every noisy data point. For this study, the determination of the smoothing parameter $p$ made a distinction between the input reference trajectories and the resulting simulation outputs. For the input biological kinematic curves, which dictate the physical actuation of the model, $p$ was determined through empirical calibration for each individual joint. This was necessary to eliminate high-frequency biological measurement noise, achieving the $C^2$ continuity required for stable electromechanical actuation without compromising the essential biological amplitudes [34].

Mathematically, the resulting curve S(t) (Equation (5)) is a piecewise cubic polynomial. For each sub-interval $[t_i, t_{i+1}]$, the localized kinematic trajectory is defined as follows:

$$S_i(t) = a_i + b_i(t - t_i) + c_i(t - t_i)^2 + d_i(t - t_i)^3 \quad (5)$$

where the coefficients $a_i$, $b_i$, $c_i$, and $d_i$ are uniquely determined by imposing continuity constraints on the function S(t), its velocity $S'(t)$, and its acceleration $S''(t)$ at the internal knots $t_i$ [33]. By extracting these polynomial coefficients, the complex, empirical biological jump was successfully translated into a finite set of explicit mathematical equations, allowing for precise computational simulation and direct integration into the robotic control architecture. For the resulting simulation output curves (such as distance and velocity), a global smoothing parameter (generally $p = 0.99999998$) was applied to mathematically characterize the results. This approach allowed the simulation outputs to be defined as formal, continuous mathematical functions rather than a collection of discrete data points, enabling a better analytical comparison. The quality of the fit was evaluated using the coefficient of determination $(R^2)$ and the Root Mean Square Error (RMSE). For brevity, the spline coefficients are omitted here as they are not directly interpretable; however, they can be provided upon request.

#### 2.1.2. Contact Parameter Considerations

To simulate the rigid bone structure, specific materials were assigned to the model components: aluminum for the limb segments (femur, tibia, and tarsus) and rubber for the metatarsus to mimic the compliance and grip of the frog's foot. The ground was modelled as American beech wood with an elastic limit of $4.55 \times 10^7$ Pa. One of the critical factors of the simulation is the coefficient of friction between the rubber metatarsus and the wooden surface, since it determines the model's ability to generate a sufficient ground reaction force without slipping [35,36]. Based on biological studies of frog behavior, a friction coefficient of $\mu = 0.7$ was selected for this study, falling within the standard range for rubber–wood contact (0.5–0.7) [21]. The material properties defined in the software are detailed in Table 5, shown below.

**Table 5.** Material properties of contact.

| | E (Pa) | Nu | Density (kg/m$^3$) | Elastic Limit (Pa) | $\alpha$ (/K) | $\lambda$ (W/(m·K)) | Cp (J/(kg·K)) |
|---|---|---|---|---|---|---|---|
| Rubber | $1.67 \times 10^7$ | $5.00 \times 10^{-1}$ | $1.25 \times 10^5$ | $1.04 \times 10^7$ | $1.75 \times 10^{-6}$ | 0.870 | $7.99 \times 10^2$ |
| Wood | $1.02 \times 10^{10}$ | $3.00 \times 10^{-1}$ | $7.125 \times 10^2$ | $4.55 \times 10^7$ | $5.40 \times 10^{-6}$ | $1.44 \times 10^{-1}$ | $3.9 \times 10^2$ |

The contact parameters were chosen to balance surface resistance and energy dissipation, using a stiffness of 10,000 N/mm and a damping coefficient of 30 Ns/mm to prevent excessive penetration and unrealistic oscillations during the impact. Furthermore, the force exponent was set to 2.2 to mimic the stiffening of biological tissues under compression; the penetration depth threshold was 0.1 mm; and the friction transition velocity was 0.1 m/s to smooth the shift between the static adhesion and dynamic sliding once the movement started. To ensure a consistent transition during these landing phases, the dynamic simulation accounts for translational and angular velocities immediately before and after ground contact. These pre- and post-impact velocities are used by the multibody solver to calculate momentum transfer and contact forces, governing the deceleration and stabilization phases of the landing.

#### 2.1.3. Kinematic Data of Joint Movement

The angular variation of the joints over time was extracted from biological graphs obtained from the study of Shuqi Wang, Jizhuang Fan, and Yubin Liu [21]. The raw data points were then interpolated using polynomial regressions and smoothing splines in MATLAB (version R2025b) to generate continuous curves suitable for driving the simulation servomotors. For instance, in Table 6, the knee joint data was fitted to a 3rd-degree polynomial with an $R^2 = 0.9998$ to ensure high fidelity to the biological movement.

**Table 6.** Polynomial equations obtained from the trajectories.

| | Degree | $R^2$ | Equation |
|---|---|---|---|
| Hip flexion | 3 | 0.9999 | $-17,297x^3 + 6458.1x^2 + 6.0916x - 0.3229$ |
| Hip abduction | 4 | 0.9971 | $68,109x^4 - 26,993x^3 + 2260.3x^2 - 88.821x - 0.4815$ |
| Hip torsion | 4 | 0.9892 | $108,048x^4 - 61,823x^3 + 10,031x^2 - 301.92x + 1.814$ |
| Knee | 3 | 0.9998 | $-20,040x^3 + 7447.2x^2 + 12.041x - 0.7565$ |
| Tarsus | 5 | 0.9962 | $2,410,867.4x^5 - 1,398,959.2x^4 + 266,868.5x^3 - 20,171.9x^2 + 536.34x - 2.66$ |

### *2.2. Smoothing of Raw Biological Data*

The system dynamics are formulated and solved using the multibody dynamics framework of Altair Inspire, which constructs and integrates the nonlinear equations of motion from the specified generalized coordinates, constraints, forces, and contact models, without requiring their explicit analytical expression. Furthermore, all motion trajectories are computed within a fixed global coordinate system, with joint motions governed directly by the imposed kinematic relationships and dynamic constraints implemented in the multibody simulation framework. The initial simulations using the raw kinematic data resulted in abrupt accelerations and energy losses due to discontinuities in the servomotor input profile curves. By applying Smoothing Spline algorithms in MATLAB, these input curves were smoothed to have less abrupt changes of rotation.

The simulation with smoothed curves (S2) improved the initial data test (S1), as seen in Figure 4 below. The model achieved a maximum horizontal distance of $d_{s2} = 26.02$ cm and a vertical height of $h_{s2} = 12.08$ cm (see Figure 5). This represents a substantial increase

compared to the initial test ($d_{s1}$ = 15.24 cm). Furthermore, the velocity profiles became continuous, eliminating the torque spikes observed in the first iteration.

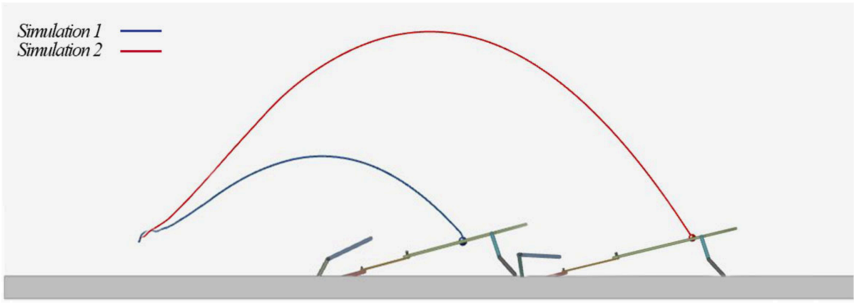
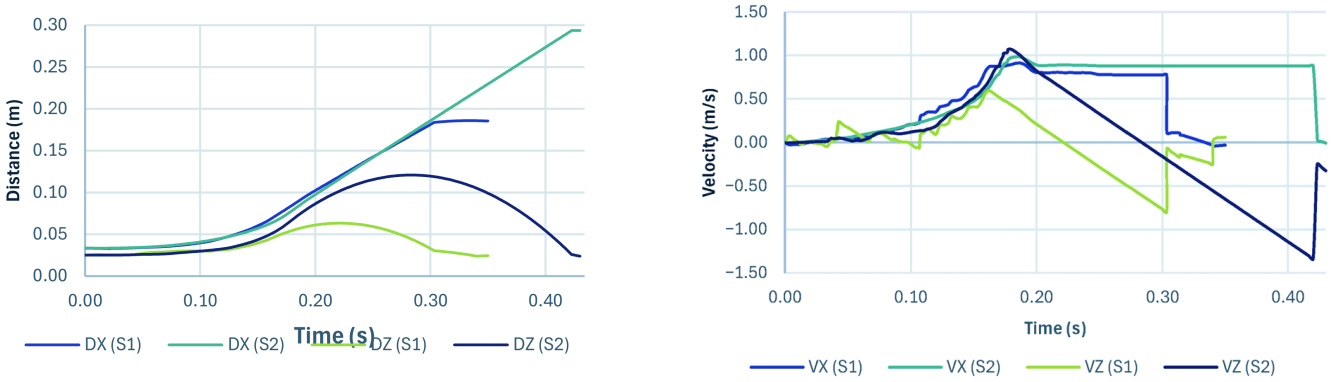



**Figure 4.** Simulation comparison with smoothed data.




(**a**) (**b**)

**Figure 5.** (**a**) Jumping distance of S1 vs. S2; (**b**) velocity of S1 vs. S2.

Table 7 presents the statistical indicators characterizing the primary kinematic curves of Figure 5. To quantify the fidelity of the optimized smoothing splines ($p$) against the raw biological data, the table reports the number of discrete points $n$; the coefficient of determination ($R^2$) to asses the overall fit quality; the absolute Root Mean Square Error (RMSE), representing the absolute angular deviation; and the Normalized RMSE (NRMSE), which expresses this error as a percentage of the joint's total range of motion. Values are rounded to three decimal places for $R^2$ and RMSE, and two decimal places for NRMSE. The complete statistical characterizations for all remaining joint trajectories are provided in Appendix A.

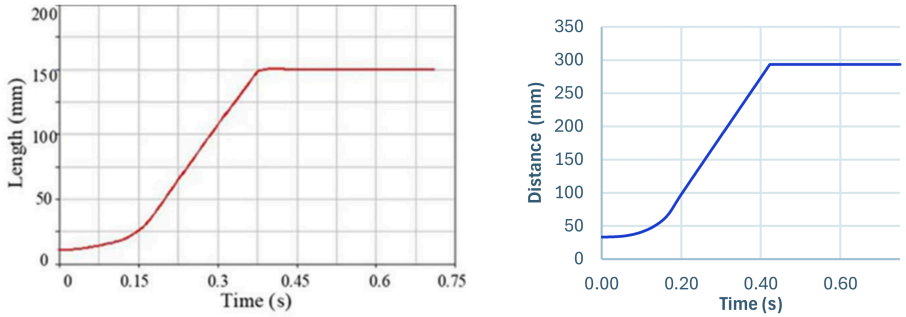
**Table 7.** Statistical indicators for CSAPS curve fitting of Figure 5.

| Curve | $R^2$ | RMSE | Normalized RMSE (%) | n |
|---|---|---|---|---|
| DX (S1) | 1.000 | $6.039 \times 10^{-5}$ | 0.04 | 130 |
| DZ (S1) | 1.000 | $7.667 \times 10^{-5}$ | 0.19 | 130 |
| DX (S2) | 1.000 | $7.080 \times 10^{-5}$ | 0.03 | 144 |
| DZ (S2) | 1.000 | $9.133 \times 10^{-5}$ | 0.09 | 144 |
| VX (S1) | 0.985 | $4.299 \times 10^{-2}$ | 4.49 | 130 |
| VZ (S1) | 0.968 | $5.297 \times 10^{-2}$ | 3.80 | 130 |
| VX (S2) | 0.993 | $3.084 \times 10^{-2}$ | 3.11 | 144 |
| VZ (S2) | 0.994 | $4.436 \times 10^{-2}$ | 1.84 | 144 |

### *2.3. Model Verification*

The simulation model was validated by comparing the results with the reference study of the Leopard frog [21], as shown in Figure 6. The replicated model's horizontal

displacement (26.02 cm) surpassed the reference value for the equivalent 6-DOF model (14 cm) and got closer to the performance of the more complex 9-DOF models (28–34 cm). For the mathematical characterization of the compared curves, see Table A1 in Appendix A.

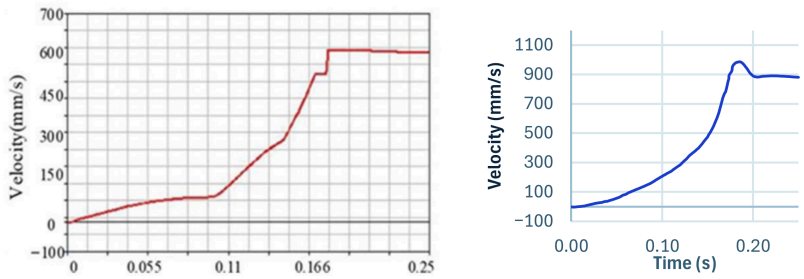



(**a**) (**b**)

**Figure 6.** Validation of the model's achieved distance compared to literature data. (**a**) Reference distance trajectory extracted from Wang et al. [21]; (**b**) simulated distance trajectory achieved by the proposed model.

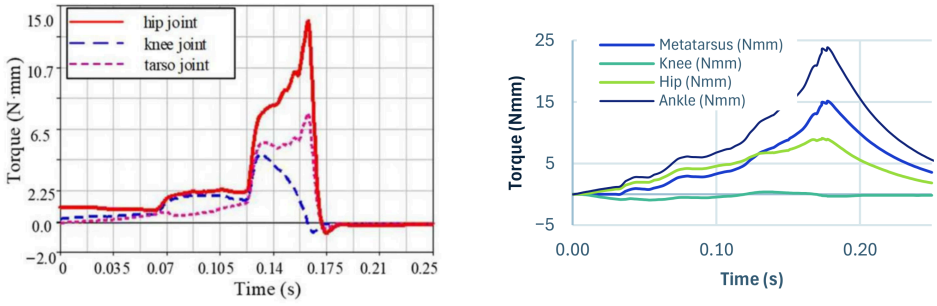
The ground reaction forces, torque, and velocity profiles also showed a strong correlation with the original data, validating the simulation setup.

The mathematical characterization of the curves shown in Figures 7 and 8 can also be seen in Table A1 in Appendix A.




(**a**) (**b**)

**Figure 7.** Validation of the model's achieved velocity compared to literature data. (**a**) Reference velocity profile extracted from [21]; (**b**) simulated velocity profile achieved by the proposed model.




(**a**) (**b**)

**Figure 8.** Validation of the model's achieved distance compared to literature data. (**a**) Reference torque extracted from [21]; (**b**) simulated torque achieved by the proposed model.

### *2.4. Simulation of the Landing Phase*

This study focuses on the inclusion of the landing phase, which is often omitted in the literature. A new kinematic model was generated by combining the take-off curves of

the biological model examined in the Leopard frog study [21] with the landing curves of the biological model of the Nigromaculata frog study [23]. Due to the limited availability of kinematic data of a continuous, full-cycle for a single species in the existing literature, combining these datasets was necessary to simulate the complete jump. However, this methodology introduces potential morphological and kinematic biases. To address this, the extracted datasets were proportionally normalized according to body length before integration. Furthermore, the application of Cubic Smoothing Splines served as the primary mathematical tool to bridge the datasets. By enforcing $C^2$ continuity across the entire trajectory, the splines mathematically guaranteed a smooth transition at the junction point between the take-off and landing datasets. This ensured kinematic compatibility and prevented any non-physical mechanical discontinuities during the subsequent multibody simulation. The final input profiles generated using this method to achieve a converging simulation are shown in Figure 9.

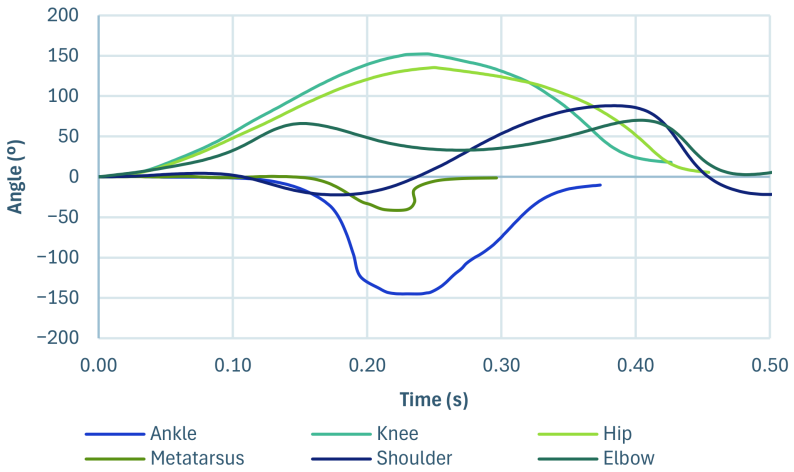



**Figure 9.** Input profile curves for the angular movement.

Geometric variation plays a fundamental role in landing stability. The position of the Centre of Gravity (COG) shifts during the flight phase. Through iterative testing, specific initial angles for the forelimbs and metatarsus were identified to ensure the robot could absorb the impact without overturning. In Table 8, the effect of variations in some of the limb positions is seen:

**Table 8.** Variance of geometry demonstration.

| | $\alpha_{tarsus}$ | $\alpha_{tibia}$ | $t_{jump}$ | Distance | Landing |
|---|---|---|---|---|---|
| **P1** | 20° | 15° | 0.4323 s | 30.49 cm |  |
| **P2** | 25° | 15° | 0.4325 s | 29.46 cm |  |
| **P3** | 28° | 15° | 0.4059 s | 24.99 cm |  |
| **P4** | 25° | 10° | 0.3394 s | 18.17 cm |  |

**Table 8.** *Cont.*

| | $\alpha_{tarsus}$ | $\alpha_{tibia}$ | $t_{jump}$ | Distance | Landing |
|---|---|---|---|---|---|
| **P5** | 25° | 13° | 0.4172 s | 28.39 cm |  |

It was found that the initial position of the head and the inclination of the torso were critical. The final dimensions shown in Figure 10 for the initial position of the frog, which provided a good COG distribution, include: a torso inclination of 5°, and a total body length (including the head) of 60 mm.

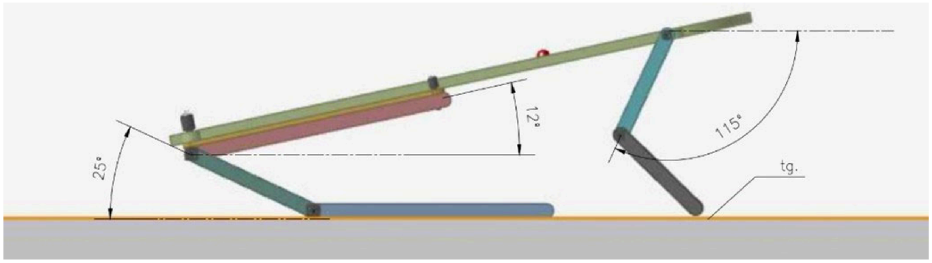



**Figure 10.** Sketch of final dimensions for the initial position.

Additionally, the initial position of the forelimbs adheres to a biological distribution with immediate contact with the ground, with a humerus angle of 115°. This allows the forelimbs to act as dampeners and absorb the kinematic energy of the landing. The detailed final dimensions can be seen in Table 9 below.

**Table 9.** Final dimensions for the initial position.

| Parameter | Value |
|---|---|
| Tibia (°) | 12° |
| Humerus (°) | 115° |
| Tarsus (°) | 25° |
| Femur (°) | 15° |
| Radius (°) | Tangent |
| Torso (°) | 5° |
| Total length | 60 mm |
| Torso length | 53 mm |
| Body width | 10 mm |

One significant challenge addressed was the stabilization of the robot after the impact. In the initial simulations, just releasing the servomotors resulted in the limbs oscillating or collapsing due to lack of stiffness and gravity. To achieve the final resting position, the data of the kinematic feedback was extracted. The motors were programmed to release the active control after the landing phase was completed ($t \approx 0.296$ s for the metatarsus), which allowed the limbs to move freely under the influence of gravity and friction dynamics. Later, using the Application Programming Interface (API) of Altair Inspire in Python (version 2024), the actual angular rotation data for the free joints was extracted. This data represented the natural equilibrium position that the robot would achieve physically. Lastly, these output values were fed back into the motor controllers as the desired input values for the simulation. This forced the motors to replicate the natural damping curve from a controlled stage. Once the model achieved the resting horizontal position at $t \approx 0.5$ s, the angular values for each joint were clamped to maintain a rigid static position, as seen in Figure 11.

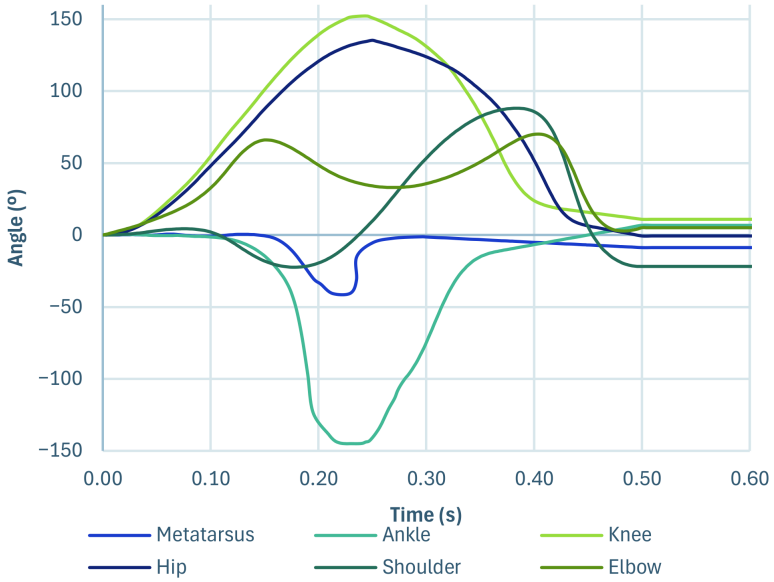



**Figure 11.** Final input curves.

## 3. Results

All dynamic evaluations and system responses presented in this section are analyzed in the time domain. Because the simulated multibody dynamics are deterministic rather than stochastic, the analysis focuses exclusively on dynamic feasibility and time-domain stability, making frequency-domain characterizations inapplicable to this scope.

In Figure 12 below, the full trajectory of the frog during all jump phases is seen in comparison with a biological specimen.

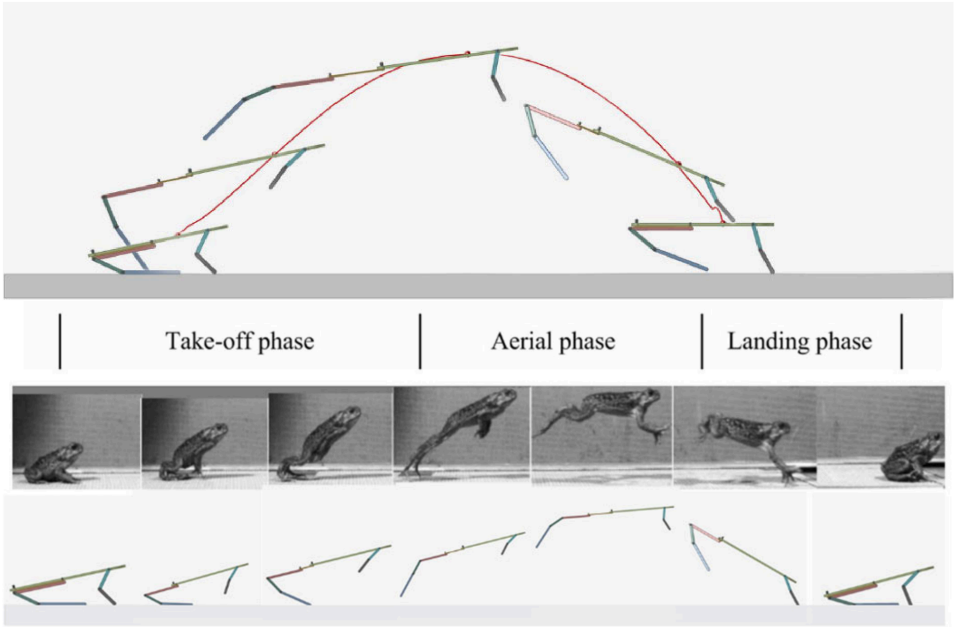



**Figure 12.** Trajectory of the simulation model vs. trajectory of a biological specimen.

The total horizontal distance achieved is $d_{s.at.2} = 24.12$ cm, and the vertical distance is $h_{s.at2} = 11.33$ cm (see Figure 13). These results have overcome the results of Model 4 from the scientific paper of Shuqi Wang, Jizhuang Fan, and Yubin Liu used as a reference [21].

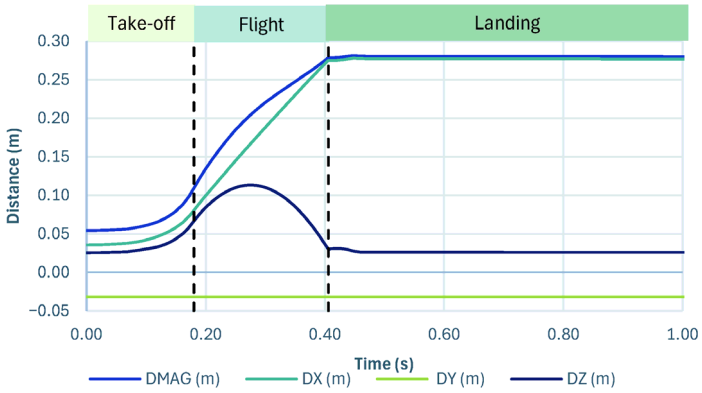



**Figure 13.** Distance achieved in the final simulation model.

The velocities obtained by the model resulted in a maximum horizontal velocity of $Vmax_{(x)}^{s.at.2} = 0.9913\ \frac{m}{s}$, and a maximum vertical velocity of $Vmax_{(z)}^{s.at.2} = 1.0014\ \frac{m}{s}$, bringing the total velocity of the frog to a maximum value of $Vmax_{(total)}^{s.at.2} = 1.45\ \frac{m}{s}$, as shown in Figure 14a.

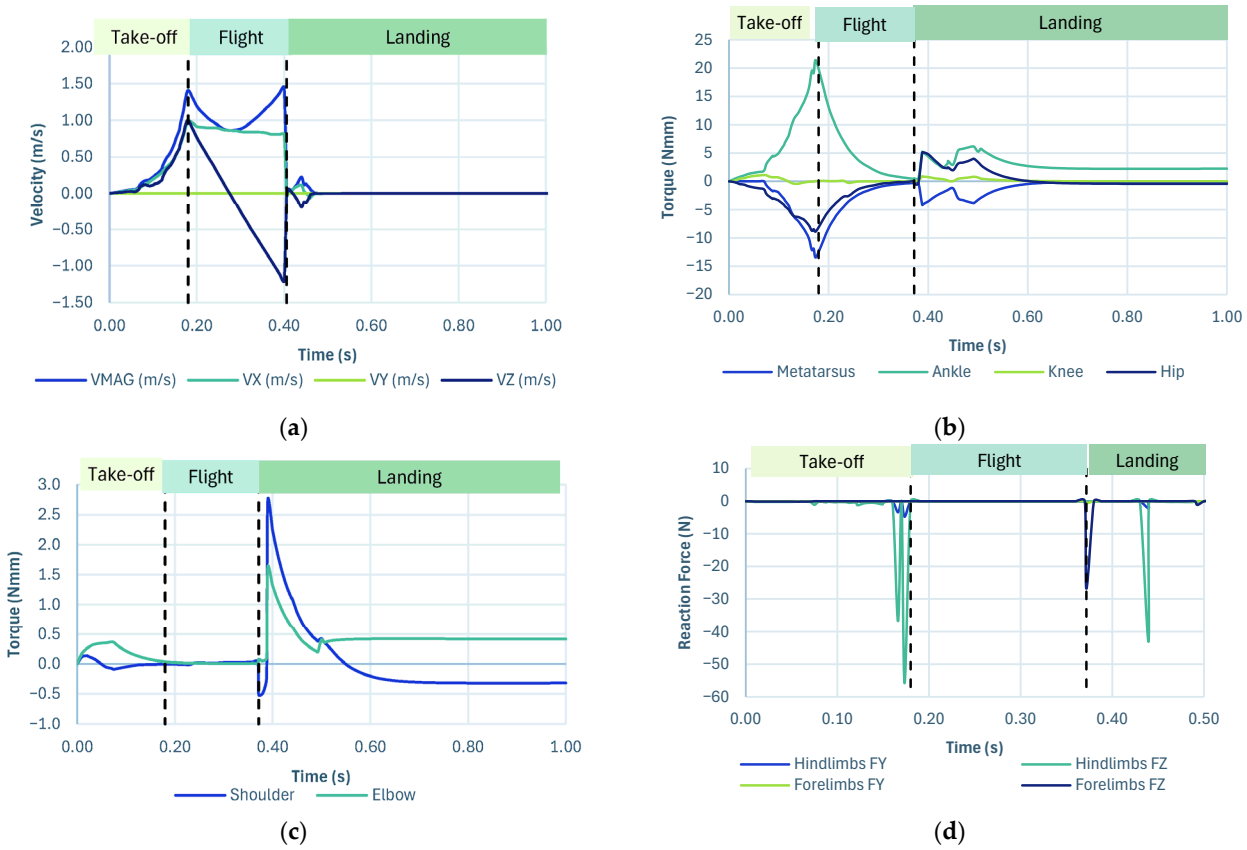



**Figure 14.** (**a**) Velocity of the final simulation model; (**b**) torque in the hind limbs; (**c**) torque in the forelimbs; (**d**) ground reaction forces.

Regarding actuator requirements (see Figure 14 above), the maximum torque was observed in the ankle joint ($Tmax_{(ankle)}^{s.at.2} = 21.416$ Nmm) and metatarsus ($Tmax_{(met)}^{s.at.2} = 13.45$ Nmm) during propulsion. The hip required $Tmax_{(hip)}^{s.at.2} = 8.885$ Nmm, and the knee $Tmax_{(knee)}^{s.at.2} = 1.121$ Nmm. In the forelimbs, the shoulder and elbow required significantly less torque ($Tmax_{(shoulder)}^{s.at.2} = 2.719$ Nmm and $Tmax_{(elbow)}^{s.at.2} = 1.612$ Nmm, respectively). The ground reaction forces from the limbs show the loading patterns during the phases of jump.

The force distribution is shown in Figure 15 below, where during take-off, the hind limbs reach a maximum vertical force of $Fmax_{(z)}^{s.at.2} = 55.85$ N and a horizontal force of $Fmax_{(x)}^{s.at.2} = 4.75$ N. In the landing phase, the impact absorbed resulted in a peak vertical force of $Fmax_{(z)}^{s.at.2} = 26.839$ N and a horizontal force of $Fmax_{(x)}^{s.at.2} = 0.633$ N. These values were obtained after refining the contact parameters. Initially, the implicit rigid stiffness coefficient (K, $K_T$) damping values (C, $C_T$) that were auto-calculated by the simulation software resulted in excessively high reaction forces due to system rigidity. To mimic a realistic flexible behavior, the stiffness was manually reduced from 50,000 N/mm to 20,000 N/mm, lowering the reaction forces to a biologically comparable range without significantly changing the motor torque profiles.

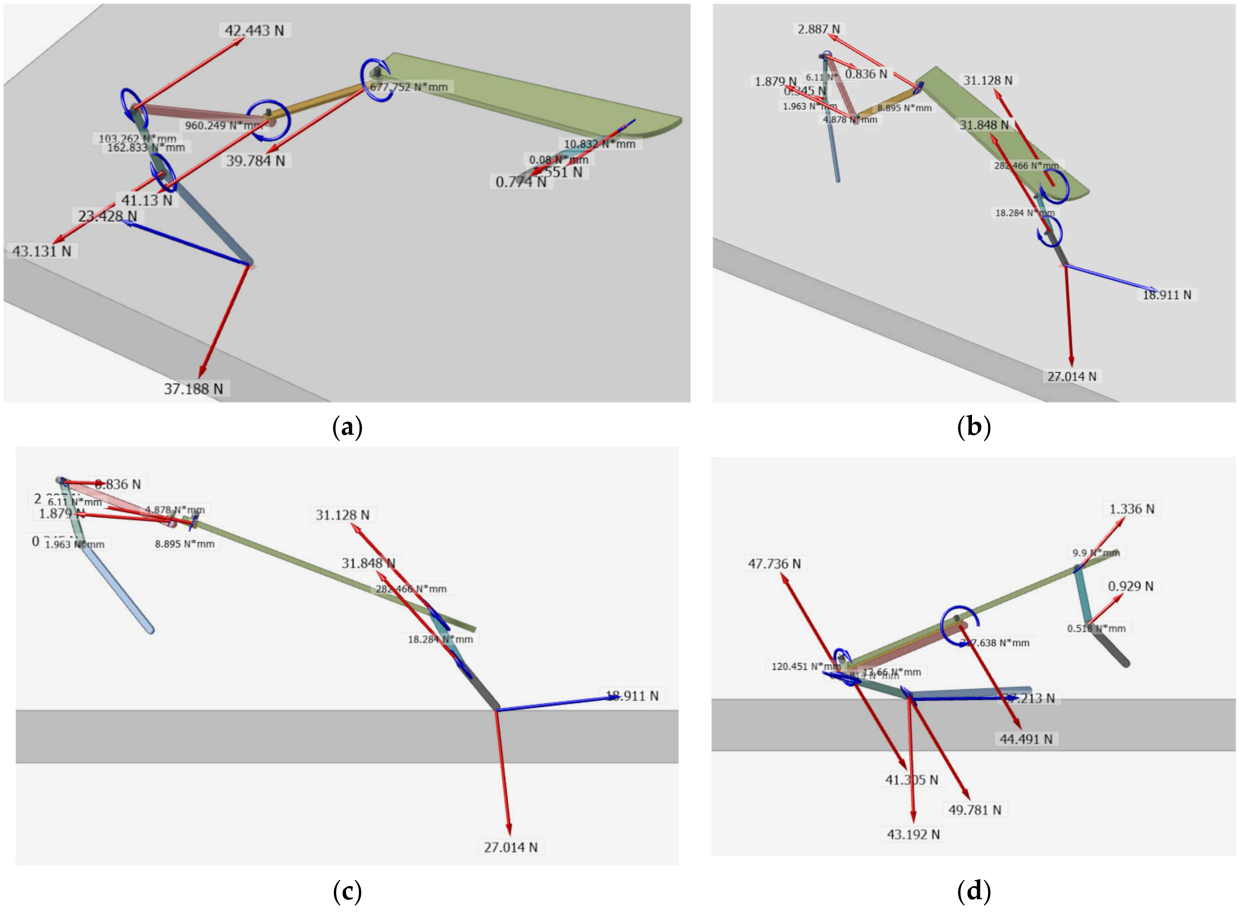
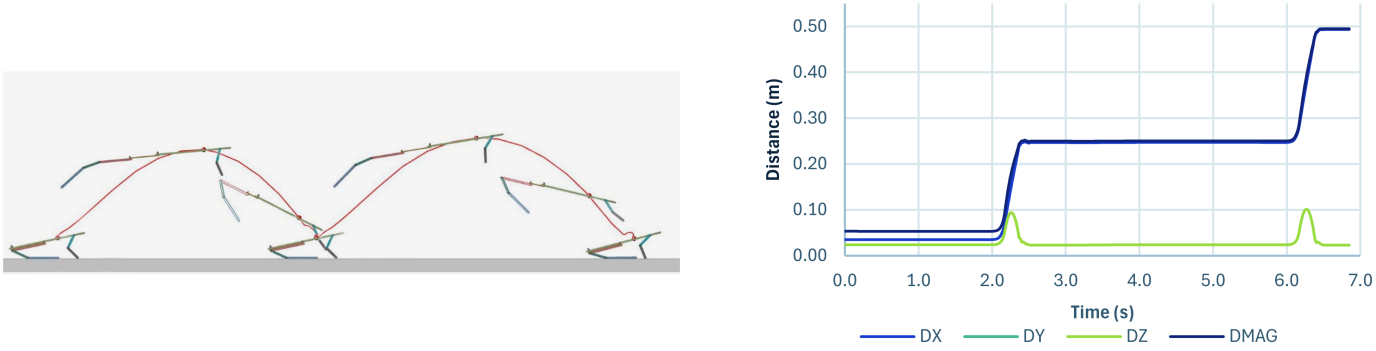



**Figure 15.** Forces diagram during the jump: (**a**) Perspective of the force diagram during the take-off phase; (**b**) perspective view of the diagram of forces during the landing phase; (**c**) diagram of forces present during the contact of the forelimbs during landing; (**d**) diagram of forces present during the contact of the hind limbs during landing.

### *3.1. Double Jump Simulation*

To demonstrate the robustness and repeatability of the model, a sequence of two consecutive jumps was simulated in Figure 16. After the first landing, the model was programmed to return to a neutral position and execute a second jump. The system successfully performed the sequence, covering a total distance of $d_{s.double\ jump} = 45.83$ cm.




(**a**) (**b**)

**Figure 16.** (**a**) Visualization of the trajectory of the model during the two jumps; (**b**) total distance achieved during the two jumps.

Due to integration errors inherent in the software, a slight variation in kinetic energy was observed between the two jumps ($E_2 > E_1$). Nevertheless, as demonstrated in Figure 17, the trajectory and energy profile remained constant, verifying the viability for continuous jumps.

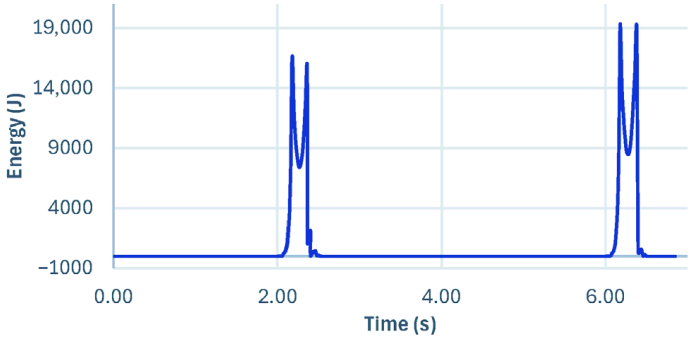



**Figure 17.** Kinetic energy of the double jump.

### *3.2. Scalability of the Model*

It is necessary to prove the scalability of the model to be able to transition the biomechanical model into a functional physical robot for future stages, since it should be adapted to accommodate real motors. In the initial model, the joint axes have diameters of merely 0.5 mm to 0.7 mm, which are geometrically accurate for a frog but too small for commercial microactuators, which typically require shaft diameters of at least 1 mm to 1.5 mm. To prove that this is possible, the geometric model was scaled to double its original size (k = 2).

This dynamic scaling process fundamentally alters the physical requirements of the system (see Equations (6) and (7)). Assuming the density (ρ) of the materials remains constant, the mass ($M$) and volume ($V$) of the robot scale cubically with respect to the geometric scale factor ($k$):

$$\rho = \frac{M}{V}; \quad \rho = \rho'; \quad k = \frac{L'}{L} \quad \rightarrow \quad V = L^3; \quad V' = (k{\cdot}L)^3; \tag{6}$$

$$\frac{M'}{M} = \frac{\rho{\cdot}V'}{\rho{\cdot}V} \rightarrow \quad M' = M{\cdot}k^3; \quad V' = V{\cdot}k^3 \tag{7}$$

Consequently, as shown in Equations (8)–(10) below, the moments of inertia are also affected. The moment of inertia with respect to the x axis is defined as:

$$I_{xx} = \int_V \rho\left(y^2 + z^2\right) dV \rightarrow \quad x' = kx,\ y' = ky,\ z' = kz \tag{8}$$

$$I'_{xx} = \int_V \rho\left(k^2y^2 + k^2z^2\right)k^3 dV \rightarrow I'_{xx} = k^5 \int_V \rho\left(y^2 + z^2\right) dV \rightarrow \quad I'_{xx} = k^5 I_{xx} \tag{9}$$

$$If\ k = 2 \rightarrow M' = 8{\cdot}M \text{ y } V' = 8{\cdot}V \text{ y } I'_{xx} = 32{\cdot}I_{xx} \tag{10}$$

Therefore, by doubling the size of the frog ($k = 2$), the model experiences an 8-fold increase in mass and a 32-fold increase in its moment of inertia. This exponential growth drastically raises the maximum torque and peak power required to actuate the robotic joints. To ensure these demands remain within the operational limits of the model, it is necessary to slow down the kinematic input curves, a modification that significantly reduces the angular velocities and, critically, the angular accelerations. To achieve this necessary reduction, the total duration of the jump was intentionally extended by 43%, increasing the execution time from 0.35 s to 0.455 s. The trajectory of the frog model can be seen in Figure 18.

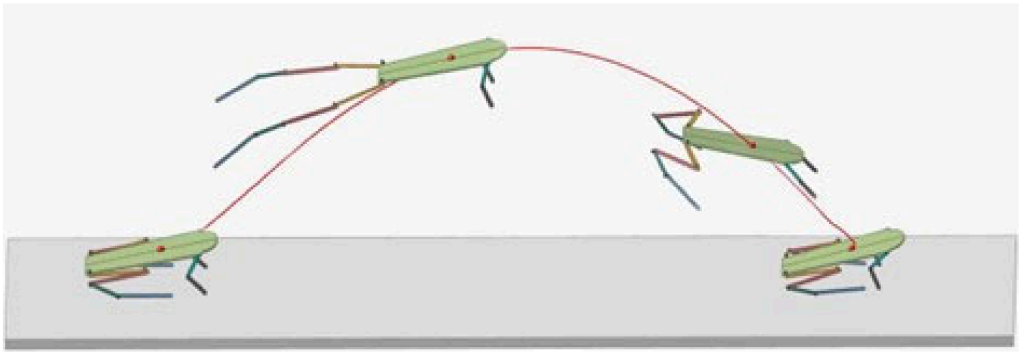
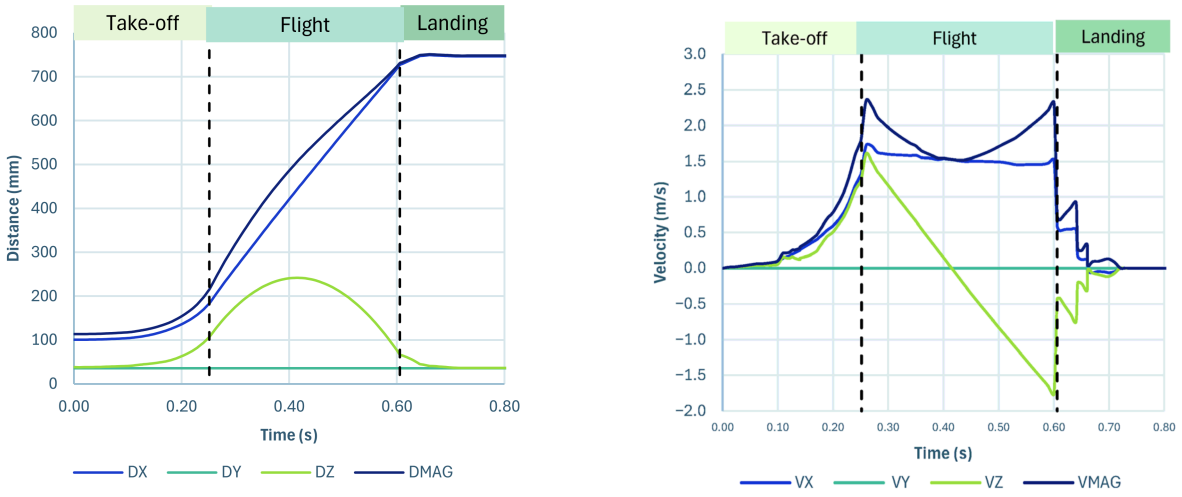


**Figure 18.** Trajectory of scaled model.

Under these adjusted parameters, the scaled model successfully achieved a maximum horizontal distance of $d_{s.motores} =$ 64.52 cm, a peak vertical height of $h_{s.motores} =$ 24.16 cm, and a maximum absolute velocity of $Vmax^{s.\ motores}_{(mag)} = 2.355\ \frac{m}{s}$ (see Figure 19), because this exponential increase in mass and inertia drastically raises the torque demanded from the joints (jumping from ~21 Nmm to ~486 Nmm).




(**a**) (**b**)

**Figure 19.** *Cont.*

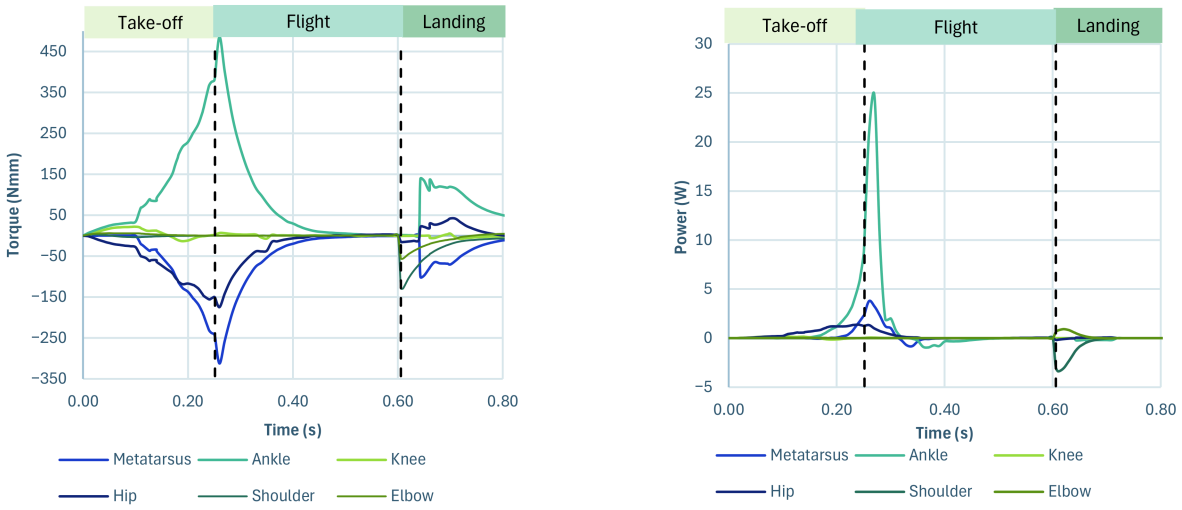



**Figure 19.** (**a**) Distance achieved in the scaled simulation model; (**b**) velocity achieved in the scaled simulation model; (**c**) torque needed for the scaled simulation model; (**d**) power needed for the scaled simulation model.

As expected and shown in Figure 20, the angular velocities decreased due to the extended jump time and the deceleration of the input curves. The limitations imposed by the required torque-to-weight ratio can be overcome in future iterations by substituting the current materials with lighter, less dense alternatives. Reducing the overall density would drastically lower the mass, torque, and power requirements, allowing commercially available DC motors with PID controllers to actuate the robotic frog.

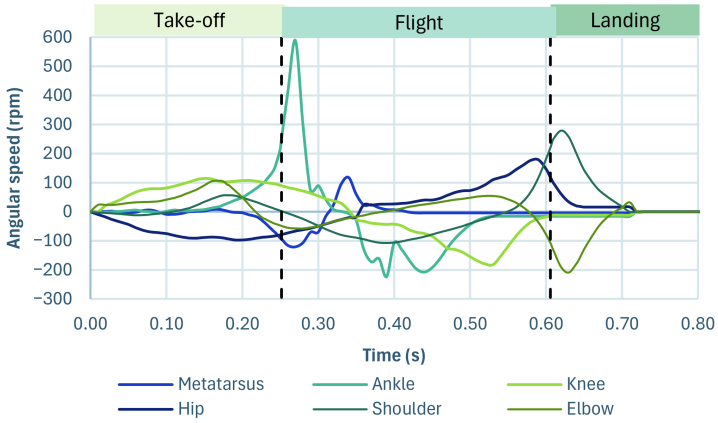



**Figure 20.** Angular velocity in the scaled model.

## 4. Discussion

This research successfully demonstrates that a biomimetic jumping framework can rely on direct servomotor actuation, effectively bypassing the need for traditional elastic energy storage. The primary objective was to design a system that precisely replicates biological kinematic trajectories through PID-controlled motors. To validate this model, the simulated joint paths were compared against the biological reference data, yielding a maximum Normalized Root Mean Square Error (NRMSE) of 4.121%. It is important to interpret this minor error as a resultant output of the dynamic interaction within the solver, rather than a forced control input. This distinction confirms that the model achieved a high-fidelity physical replication of biological motion and maintained mechanical continuity across all jump phases.

One of the major contributions of this work is the synchronization of disparate biological datasets to model the landing phase, a stage often overlooked in literature due to a lack of documented kinematics. The unified model achieved a horizontal distance of 24.12 cm (4.02 body lengths (BLs)) and a maximum height of 11.33 cm. Even though this represents a 14.86% improvement over simplified six-DOF models found in the existing literature [21], this is a reduction compared to high-fidelity nine-DOF models (which reach 8.5 BLs) [21]. This highlights an inherent engineering trade-off. Our results suggest that while six-DOF models provide computational efficiency and sufficient stability for landing, they sacrifice a degree of the propulsive complexity seen in higher-order biological models.

By accepting this propulsive trade-off in favor of continuous PID control, the system gains significant robustness. This was validated by simulating a continuous double jump. Furthermore, force and velocity analyses demonstrated that the system correctly mimics biological impact absorption, properly distributing landing stresses between the forelimbs and hind limbs.

These findings offer a counter perspective in the field, since the majority of previous studies have relied on energy storage systems to mimic the catapult systems of frogs. For instance, models using Spring-Loaded Inverted Pendulums (SLIPs), soft body detonation drives, and pneumatic muscle actuators (PMAs) demonstrate excellent take-off velocities and high power-to-weight ratios. However, systems relying on instantaneous energy release suffer from unpredictable dynamics, making continuous trajectory control and stabilization during the landing phase difficult. By prioritizing joint controllability over explosive power, this study replaces springs with servomotors. Eliminating the erratic bounce associated with passive elastic elements allows the PID controllers to manage the deceleration of the center of gravity, preventing the forward destabilization observed in early simulation iterations (see Table 8 and Figure 15).

While the current scaled model effectively demonstrates stable jumping and landing in a simulated environment, certain limitations must be acknowledged. Biological organisms evolved their power density at a very specific micro scale. When translating these biological principles to a macro robotic scale, the mass of batteries, controllers, and DC motors must be accounted for. A direct 1:1 mapping of biological kinematics is often physically impossible without exceeding the torque limits of commercially available actuators, and the non-linear scaling laws of physics should be followed. Consequently, future physical prototyping should prioritize material exploration. The current simulation's reliance on standard material densities contributes heavily to the high torque demands, which required a decelerated jump. Integrating low-density materials like carbon fiber composites or advanced 3D-printed thermoplastics will reduce the structural mass and moment of inertia. This reduction will alleviate the torque burden, allowing physical servomotors to execute kinematic curves at speeds closer to the biological baseline.

A methodological limitation of this study is the reliance on combined kinematic data from two distinct frog species to construct the complete jump trajectory. Although the proportional normalization of the data and the application of $C^2$ continuous splines successfully guaranteed mechanical feasibility and numerical stability at the junction point, subtle inter-species variations in morphological coupling or energy transfer may not be fully captured. While this mathematical model proves dynamically robust for initial robotic design and control validation, future experimental validation and physical prototyping should ideally rely on full-cycle kinematic data extracted from a single species. This will further refine the biological fidelity of the robotic system and eliminate potential cross-species morphological bias.

Beyond these biological data constraints, simulating multi-cycle locomotion presents significant computational challenges. The non-linear contact dynamics during high-velocity

landings cause inherent convergence instabilities in the multibody solver. Over multiple cycles, these compounding numerical errors make it very hard to isolate genuine physical energy drift from software failures. Consequently, the simulation was deliberately restricted to two consecutive jumps. This validates the most critical phase, energy dissipation during landing and immediate re-stabilization, while avoiding cumulative solver errors. Assessing true long-term repeatability and energy loss will require a physical prototype to bypass numerical and morphological limitations. Indeed, a primary limitation of the current study is the absence of a physical prototype. Because the scope of this research is confined to mathematical modeling and multibody dynamic simulation, the system is validated numerically against biological kinematic datasets rather than through physical experimentation. Experimental implementation and empirical validation of the contact forces and trajectory tracking remain a critical next step for future work.

Additionally, the current dynamic model assumes a perfectly rigid take-off surface. Since substrate compliance plays a critical role in energy transfer efficiency during the take-off phase [37], its effects must be investigated. Future iterations of this research should explore the implementation of adaptive PID control strategies to adjust with surface stiffnesses and ensure that the robot maintains good take-off and landing stability across diverse and unpredictable terrains.

## 5. Conclusions

The primary original contribution of this research is the development of a fully continuous mathematical and dynamic framework for bio-inspired jumping that relies exclusively on active servomotor control, successfully challenging the prevailing reliance on elastic energy storage. Unlike previous studies that focus primarily on explosive take-off using passive mechanical springs, this novel approach explicitly solves the mathematically complex problem of landing stabilization. By mathematically characterizing biological kinematic data through Cubic Smoothing Splines, the inherent noise from the biological datasets was translated into continuous trajectories. This continuity is what enables the PID servomotors to track the movement without numerical destabilization during the simulation. This created a stable dynamic model capable of executing both take-off and landing phases, achieving a horizontal distance of 24.12 cm, while mitigating the destabilizing impacts associated with energy release systems.

Although transitioning from a biological micro-scale to a robotic macro-scale increases structural mass and joint torques, the necessary deceleration of the kinematic curves reduces these dynamic demands and accounts for the prolonged flight time. By pairing this temporal optimization with the future integration of low-density materials, the system's torque requirements can be managed within the operational limits of commercial actuators. Ultimately, this research presents a continuous mathematical and dynamic framework for bio-inspired jumping. By proving that joint control can serve as an alternative to passive elasticity, this work provides a foundation for the future physical fabrication of controllable, multi-terrain jumping robots capable of continuous locomotion.

**Author Contributions:** Conceptualization, J.D.C.-M. and N.S.P.; methodology, J.D.C.-M. and N.S.P.; software, J.D.C.-M. and N.S.P.; validation, J.D.C.-M. and N.S.P.; formal analysis, J.D.C.-M. and N.S.P.; investigation, J.D.C.-M. and N.S.P.; data curation, J.D.C.-M. and N.S.P.; writing—original draft preparation, N.S.P.; writing—review and editing, J.D.C.-M. and N.S.P.; visualization, J.D.C.-M. and N.S.P.; supervision, J.D.C.-M. All authors have read and agreed to the published version of the manuscript.

**Funding:** This research received no external funding.

**Data Availability Statement:** The original contributions presented in this study are included in the article. Further inquiries can be directed to the corresponding author.

**Conflicts of Interest:** The authors declare no conflicts of interest.

## Abbreviations

The following abbreviations are used in this manuscript:

| | |
|---|---|
| API | Application Programming Interface |
| BL | Body length |
| COG | Center of gravity |
| CSAPS | Cubic Smoothing Splines |
| DOF | Degrees of freedom |
| HIT | Harbin Institute of Technology |
| NRMSE | Normalized Root Mean Square Error |
| PID | Proportional–Integral–Derivative |
| PMA | Pneumatic muscle actuator |
| PWM | Pulse Width Modulation |
| RMSE | Root Mean Square Error |
| SLIP | Spring-Loaded Inverted Pendulum |
| SMAs | Shape Memory Alloys |

## Appendix A

This appendix provides the detailed statistical indicators for the CSAPS curve fitting of all curves discussed in Sections 2 and 3.

**Table A1.** Statistical indicators of the CSAPS curve fitting for the curves compared with the literature in Figures 6–8.

| Curve | $R^2$ | RMSE | Normalized RMSE (%) | n |
|---|---|---|---|---|
| Dx | 1 | 0 | 0 | 272 |
| Vx | 0.993 | 30.837 | 3.11 | 144 |
| Torque (Ankle) | 1 | 0.0974 | 0.408 | 144 |
| Torque (Metatarsus) | 1 | 0.0646 | 0.427 | 144 |
| Torque (Knee) | 0.998 | 0.0125 | 0.957 | 144 |
| Torque (Hip) | 1 | 0.0342 | 0.375 | 144 |

**Table A2.** Statistical indicators of the CSAPS curve fitting for the input curves for angular movement in Figure 9.

| Curve | $R^2$ | RMSE | Normalized RMSE (%) | n |
|---|---|---|---|---|
| Metatarsus | 0.9774 | 1.6977 | 4.121 | 47 |
| Ankle | 0.9999 | 0.3906 | 0.269 | 79 |
| Knee | 1 | 0.0231 | 0.015 | 96 |
| Hip | 1 | 0.0331 | 0.024 | 105 |
| Shoulder | 1 | 0.0177 | 0.016 | 121 |
| Elbow | 1 | 0.0182 | 0.026 | 121 |

**Table A3.** Statistical indicators of the CSAPS curve fitting for the final input of the angular movement of the joints in Figure 11.

| Curve | $R^2$ | RMSE | Normalized RMSE (%) | n |
|---|---|---|---|---|
| Metatarsus | 0.979 | 1.0169 | 2.469 | 131 |
| Ankle | 0.9999 | 0.4828 | 0.318 | 131 |
| Knee | 0.9999 | 0.444 | 0.292 | 131 |
| Hip | 0.9999 | 0.3753 | 0.276 | 131 |

**Table A3.** *Cont.*

| Curve | $R^2$ | RMSE | Normalized RMSE (%) | n |
|---|---|---|---|---|
| Shoulder | 1 | 0.0152 | 0.014 | 177 |
| Elbow | 1 | 0.0237 | 0.034 | 177 |

**Table A4.** Statistical indicators of the CSAPS curve fitting for the distance, velocity, torque, and reaction forces achieved in the final simulation model and described in Figures 13 and 14.

| Curve | $R^2$ | RMSE | Normalized RMSE (%) | n |
|---|---|---|---|---|
| DMAG (m) | 1 | 0 | 0.016 | 219 |
| DX (m) | 1 | 0 | 0.018 | 219 |
| DY (m) | 0.9982 | 0 | 0.617 | 219 |
| DZ (m) | 1 | 0.0001 | 0.082 | 219 |
| VMAG (m/s) | 0.9949 | 0.026 | 1.795 | 219 |
| VX (m/s) | 0.9968 | 0.016 | 1.526 | 219 |
| VY (m/s) | 0.6493 | 0 | 3.962 | 219 |
| VZ (m/s) | 0.9935 | 0.0203 | 0.918 | 219 |
| Torque (Metatarsus) | 0.9986 | 0.1112 | 0.826 | 118 |
| Torque (Ankle) | 0.9986 | 0.1637 | 0.764 | 118 |
| Torque (Knee) | 0.9959 | 0.0212 | 1.386 | 118 |
| Torque (Hip) | 0.9986 | 0.1043 | 0.744 | 118 |
| Torque (Shoulder) | 0.9134 | 0.1475 | 4.566 | 118 |
| Torque (Elbow) | 0.9074 | 0.0761 | 4.719 | 118 |
| Forelimbs FY * | 0.8491 | 0.0226 | 3.537 | 118 |
| Forelimbs FZ * | 0.8479 | 0.9582 | 3.57 | 118 |

*: A higher smoothing parameter ($p = 0.999999998$) was applied to the reaction force curves. Unlike the kinematic joint trajectories, which require mathematical smoothing for continuous PID control, the reaction forces are resultant simulation outputs. Therefore, prioritizing data fidelity (higher $p$) is necessary to accurately capture the high-frequency impact peaks of the jump.

**Table A5.** Statistical indicators of the CSAPS curve fitting for the distance achieved and described in Figure 16, and the kinetic energy of both jumps as described in Figure 17, for the double jump simulation.

| Curve | $R^2$ | RMSE | Normalized RMSE (%) | n |
|---|---|---|---|---|
| DX | 1 | 0 | 0.005 | 364 |
| DY | 0.998 | 0 | 0.541 | 364 |
| DZ | 1 | 0 | 0.056 | 364 |
| DMAG | 1 | 0 | 0.004 | 364 |
| Energy | 0.994 | 248 | 1.28 | 364 |

**Table A6.** Statistical indicators of the CSAPS curve fitting for the distance, velocity, torque, and power required in the scaled model described in Figure 19.

| Curve | $R^2$ | RMSE | Normalized RMSE (%) | n |
|---|---|---|---|---|
| DX | 1 | 0.086 | 0.013 | 167 |
| DY | 0.9984 | 0 | 0.752 | 167 |
| DZ | 1 | 0.1234 | 0.06 | 167 |
| DMAG | 1 | 0.0786 | 0.012 | 167 |
| VX | 0.9985 | 0.0242 | 1.353 | 167 |
| VY * | 0.8167 | 0.0001 | 3.112 | 167 |
| VZ | 0.9949 | 0.0376 | 1.119 | 167 |
| VMAG | 0.9967 | 0.0434 | 1.845 | 167 |
| Torque (Metatarsus) | 0.9962 | 3.7834 | 1.21 | 167 |
| Torque (Ankle) | 0.9963 | 5.4925 | 1.129 | 167 |
| Torque (Knee) | 0.997 | 0.3191 | 0.899 | 167 |
| Torque (Hip) | 0.9988 | 1.4872 | 0.686 | 167 |
| Torque (Shoulder) | 0.9808 | 2.7225 | 2.064 | 167 |
| Torque (Elbow) | 0.9867 | 1.1641 | 1.865 | 167 |

**Table A6.** *Cont.*

| Curve | $R^2$ | RMSE | Normalized RMSE (%) | n |
|---|---|---|---|---|
| Power (Metatarsus) | 0.9989 | 0.0183 | 0.398 | 167 |
| Power (Ankle) | 0.9984 | 0.1137 | 0.443 | 167 |
| Power (Knee) | 0.9996 | 0.0011 | 0.313 | 167 |
| Power (Hip) | 0.9996 | 0.0073 | 0.47 | 167 |
| Power (Shoulder) | 0.9863 | 0.0563 | 1.653 | 167 |
| Power (Elbow) | 0.994 | 0.0106 | 1.128 | 167 |

*: Due a better fit and maintaining a Normalized RMSE (%), the smoothing parameter ($p$) was increased to $p = 0.999999998$ for the curve VY.

**Table A7.** Statistical indicators of the CSAPS curve fitting for the angular speed in the scaled model described in Figure 20.

| Curve | $R^2$ | RMSE | Normalized RMSE (%) | n |
|---|---|---|---|---|
| Metatarsus | 0.999 | 0.805 | 0.337 | 167 |
| Ankle | 0.998 | 3.513 | 0.433 | 167 |
| Knee | 1 | 0.328 | 0.111 | 167 |
| Hip | 1 | 0.501 | 0.182 | 167 |
| Shoulder | 1 | 0.234 | 0.061 | 167 |
| Elbow | 1 | 0.537 | 0.17 | 167 |

## References


1. Müller, E. Science and Skiing. In *Proceedings of the 1st International Congress on Skiing and Science, Sankt Christoph am Arlberg, Austria, 7–13 January 1996*, 1st ed.; E & FN Spon: London, UK; New York, NY, USA, 2003; ISBN 978-0-203-47617-8.
2. Amersdorfer, M.; Meurer, T. Equidistant Tool Path and Cartesian Trajectory Planning for Robotic Machining of Curved Freeform Surfaces. *IEEE Trans. Automat. Sci. Eng.* **2022**, *19*, 3311–3323. [CrossRef]
3. Vincent, J.F.V.; Bogatyreva, O.A.; Bogatyrev, N.R.; Bowyer, A.; Pahl, A.-K. Biomimetics: Its Practice and Theory. *J. R. Soc. Interface* **2006**, *3*, 471–482. [CrossRef] [PubMed]
4. Bhushan, B. Biomimetics: Lessons from Nature—An Overview. *Phil. Trans. R. Soc. A* **2009**, *367*, 1445–1486. [CrossRef] [PubMed]
5. Wagner, P.; Fürstner, R.; Barthlott, W.; Neinhuis, C. Quantitative Assessment to the Structural Basis of Water Repellency in Natural and Technical Surfaces. *J. Exp. Bot.* **2003**, *54*, 1295–1303. [CrossRef]
6. Niewiarowski, P.H.; Stark, A.Y.; Dhinojwala, A. Sticking to the Story: Outstanding Challenges in Gecko-Inspired Adhesives. *J. Exp. Biol.* **2016**, *219*, 912–919. [CrossRef]
7. Arzt, E.; Gorb, S.; Spolenak, R. From Micro to Nano Contacts in Biological Attachment Devices. *Proc. Natl. Acad. Sci. USA* **2003**, *100*, 10603–10606. [CrossRef]
8. Bechert, D.W.; Bruse, M.; Hage, W.; Meyer, R. Fluid Mechanics of Biological Surfaces and Their Technological Application. *Naturwissenschaften* **2000**, *87*, 157–171. [CrossRef]
9. Yang, C.-M.; Hung, J.-Y.; Wang, Y.-L.; Lien, Y.-H. Analysis of Mercedes-Benz Concept Car Using Biomimicry Design Spiral and Template Analysis—An Exploratory Study. *Int. J. Innov. Manag.* **2019**, *7*, 49–56.
10. Efstathiadis, A.; Symeonidou, I.; Tzimtzimis, E.K.; Avtzis, D.; Tsongas, K.; Tzetzis, D. Parametric Design and Mechanical Characterization of a Selective Laser Sintering Additively Manufactured Biomimetic Ribbed Dome Inspired by the Chorion of Lepidopteran Eggs. *Biomimetics* **2024**, *10*, 1. [CrossRef]
11. Dai, X.; Chi, X.; Pan, L.; Zhou, H.; Wu, Q.; Hu, Z.; Wang, J. Design and Experimental Study of Octopus-Inspired Soft Underwater Robot with Integrated Walking and Swimming Modes. *Biomimetics* **2026**, *11*, 59. [CrossRef]
12. Zhang, C.; Zou, W.; Ma, L.; Wang, Z. Biologically Inspired Jumping Robots: A Comprehensive Review. *Robot. Auton. Syst.* **2020**, *124*, 103362. [CrossRef]
13. Mo, X.; Ge, W.; Miraglia, M.; Inglese, F.; Zhao, D.; Stefanini, C.; Romano, D. Jumping Locomotion Strategies: From Animals to Bioinspired Robots. *Appl. Sci.* **2020**, *10*, 8607. [CrossRef]
14. Jung, G.-P.; Casarez, C.S.; Jung, S.-P.; Fearing, R.S.; Cho, K.-J. An Integrated Jumping-Crawling Robot Using Height-Adjustable Jumping Module. In *Proceedings of the 2016 IEEE International Conference on Robotics and Automation (ICRA), Stockholm, Sweden, 16–21 May 2016*; IEEE: Piscataway, NJ, USA, 2016; pp. 4680–4685.
15. Kovac, M.; Fuchs, M.; Guignard, A.; Zufferey, J.-C.; Floreano, D. A Miniature 7g Jumping Robot. In *Proceedings of the 2008 IEEE International Conference on Robotics and Automation, Pasadena, CA, USA, 19–23 May 2008*; IEEE: Piscataway, NJ, USA, 2008; pp. 373–378.

16. Sprowitz, A.; Gottler, C.; Sinha, A.; Caer, C.; Ooztekin, M.U.; Petersen, K.; Sitti, M. Scalable Pneumatic and Tendon Driven Robotic Joint Inspired by Jumping Spiders. In *Proceedings of the 2017 IEEE International Conference on Robotics and Automation (ICRA), Singapore, 29 May–3 June 2017*; IEEE: Piscataway, NJ, USA, 2017; pp. 64–70.
17. Ni, F.; Rojas, D.; Tang, K.; Cai, L.; Asfour, T. A Jumping Robot Using Soft Pneumatic Actuator. In *Proceedings of the 2015 IEEE International Conference on Robotics and Automation (ICRA), Seattle, WA, USA, 26–30 May 2015*; IEEE: Piscataway, NJ, USA, 2015; pp. 3154–3159.
18. Koh, J.-S.; Jung, S.-P.; Noh, M.; Kim, S.-W.; Cho, K.-J. Flea Inspired Catapult Mechanism with Active Energy Storage and Release for Small Scale Jumping Robot. In *Proceedings of the 2013 IEEE International Conference on Robotics and Automation, Karlsruhe, Germany, 6–10 May 2013*; IEEE: Piscataway, NJ, USA, 2013; pp. 26–31.
19. Jung, G.-P.; Cho, K.-J. Froghopper-Inspired Direction-Changing Concept for Miniature Jumping Robots. *Bioinspir. Biomim.* **2016**, *11*, 056015. [CrossRef] [PubMed]
20. Tolley, M.T.; Shepherd, R.F.; Karpelson, M.; Bartlett, N.W.; Galloway, K.C.; Wehner, M.; Nunes, R.; Whitesides, G.M.; Wood, R.J. An Untethered Jumping Soft Robot. In *Proceedings of the 2014 IEEE/RSJ International Conference on Intelligent Robots and Systems, Chicago, IL, USA, 14–18 September 2014*; IEEE: Piscataway, NJ, USA, 2014; pp. 561–566.
21. Wang, S.; Fan, J.; Liu, Y. Simulation Analysis of Frog-Inspired Take-Off Performance Based on Different Structural Models. *Biomimetics* **2024**, *9*, 168. [CrossRef]
22. Azizi, E.; Roberts, T.J. Muscle Performance during Frog Jumping: Influence of Elasticity on Muscle Operating Lengths. *Proc. Biol. Sci.* **2010**, *277*, 1523–1530. [CrossRef]
23. Wang, M.; Zang, X.; Fan, J.; Zhao, J. Biological Jumping Mechanism Analysis and Modeling for Frog Robot. *J. Bionic Eng.* **2008**, *5*, 181–188. [CrossRef]
24. Fan, J.; Du, Q.; Dong, Z.; Zhao, J.; Xu, T. Design of the Jump Mechanism for a Biomimetic Robotic Frog. *Biomimetics* **2022**, *7*, 142. [CrossRef]
25. Kargo, W.J.; Nelson, F.; Rome, L.C. Jumping in Frogs: Assessing the Design of the Skeletal System by Anatomically Realistic Modeling and Forward Dynamic Simulation. *J. Exp. Biol.* **2002**, *205*, 1683–1702. [CrossRef]
26. Gao, Z. Bionics-Based Research on Frog-Jumping Robots. *Highlights Sci. Eng. Technol.* **2025**, *149*, 147–154. [CrossRef]
27. Zhong, J.; Luo, M.; Liu, X.; Fan, J.; Zhao, J. Frog-Inspired Jumping Robot Actuated by Pneumatic Muscle Actuators. *Adv. Mech. Eng.* **2018**, *10*, 1687814018782303. [CrossRef]
28. Pan, Y.; Fan, J.; Ma, W.; Gao, F.; Liu, G.; Zhao, J. Design and Motion Analysis of a Frog-like Jumping Robot Based on a Soft Body Detonation Drive. *Mater. Des.* **2023**, *232*, 112127. [CrossRef]
29. Pérez, N.L.Q.; Durandal, E.C. Sistema de control de mano robótica replicadora de movimientos para manipular sustancias químicas. *Acta Nova* **2019**, *9*, 82–114.
30. Bhandari, A.S.; Chaudhuri, A.; Sharad, M. Single Chip Self-Tunable N-Input N-Output PID Control System with Integrated Analog Front-End for Miniature Robotics. *arXiv* **2016**, arXiv:1611.05164.
31. Franklin, G.F.; Powell, J.D.; Emami-Naeini, A. *Feedback Control of Dynamic Systems*, 6th ed.; Pearson: Upper Saddle River, NJ, USA, 2010; ISBN 978-0-13-601969-5.
32. Peón-Escalante, R.; Flota-Bañuelos, M.; Quintal-Palomo, R.; Ricalde, L.J.; Peñuñuri, F.; Jiménez, B.C.; Viñas, J.A. Neural Network Based Control of Four-Bar Mechanism with Variable Input Velocity. *Mathematics* **2023**, *11*, 2148. [CrossRef]
33. Csaps-Cubic Smoothing Spline-MATLAB. Available online: https://nl.mathworks.com/help/curvefit/csaps.html (accessed on 17 March 2026).
34. Yuan, Y.; Li, J.; Yu, Q.; Liu, J.; Li, Z.; Li, Q.; Liu, N. A Two-Stage Facial Kinematic Control Strategy for Humanoid Robots Based on Keyframe Detection and Keypoint Cubic Spline Interpolation. *Mathematics* **2024**, *12*, 3278. [CrossRef]
35. Overview of Materials for Silicone Rubber. Available online: https://www.matweb.com/search/datasheet.aspx?MatGUID=cbe7a469897a47eda563816c86a73520 (accessed on 2 December 2024).
36. American Beech Wood. Available online: https://www.matweb.com/search/DataSheet.aspx?MatGUID=6556531a678c405f86cd9412f8fa8f61 (accessed on 27 December 2024).
37. Zhou, R.; Zhang, B.; Wang, Z.; Dai, Z. Effect of Substrate Compliance on the Jumping Mechanism of the Tree Frog (*Polypedates dennys*). *Biomimetics* **2025**, *10*, 604. [CrossRef]


**Disclaimer/Publisher's Note:** The statements, opinions and data contained in all publications are solely those of the individual author(s) and contributor(s) and not of MDPI and/or the editor(s). MDPI and/or the editor(s) disclaim responsibility for any injury to people or property resulting from any ideas, methods, instructions or products referred to in the content.